PHYSICAL REVIEW RESEARCH **7**, 013152 (2025)

Layered aquatic microenvironments control fluctuations generated by active carpets

Felipe A. Barros ,[1,*] Hugo N. Ulloa ,[2,†] Gabriel Aguayo ,[3,‡] Arnold J. T. M. Mathijssen ,[4,§]
and Francisca Guzmán-Lastra [5,‖]

[1]*Departamento de Física, Facultad de Ciencias Físicas y Matemáticas, Universidad de Concepción, 4070386 Concepción, Chile*
[2]*Department of Earth and Environmental Science, University of Pennsylvania, Philadelphia, Pennsylvania 19104-6316, USA*
[3]*Departamento de Física, Facultad de Ciencias Físicas y Matemáticas, Universidad de Chile, 7800003 Santiago, Chile*
[4]*Department of Physics and Astronomy, University of Pennsylvania, Philadelphia, Pennsylvania 19104-6316, USA*
[5]*Departamento de Física, Facultad de Ciencias, Universidad de Chile, 7800003 Santiago, Chile*

(Received 11 April 2024; accepted 6 January 2025; published 12 February 2025)

In Earth's aquatic environments and the human body, microbial swimmers often accumulate at interfaces within layered systems, forming colonies known as *active carpets*. These bioactive layers enhance mass transport and diffusion in fluid media. Here we study the hydrodynamic behavior induced by *active carpets* within confined semi-infinite fluid layers, such as the one found in the sea surface microlayer. By deriving analytical expressions and performing numerical simulations, we explore how geometrical and viscous confinement (layer thickness and viscosity ratio) influence hydrodynamic fluctuations and passive tracer dynamics. Our findings reveal anisotropic distributions of fluctuations, characterized by three distinct regions: near the *active carpet* and fluid-fluid interface (Region I), vertical fluctuations dominate; in an intermediate region (Region II), fluctuations become isotropic; and near the free surface (Region III), horizontal fluctuations prevail. The results also demonstrate the emergence of coherent vortical structures in highly confined systems, with roll-like patterns governed by the thickness of the confined layer and the sharpness in viscosity transitions. The insights provided by this work have implications for understanding biogenic flow patterns and transport processes in natural and engineered environments, offering potential applications in areas such as microbial ecology, biofilm management, and microfluidic technologies.

DOI: 10.1103/PhysRevResearch.7.013152

I. INTRODUCTION

In nature, biological activity is often densely concentrated and covers large areas on solid or soft surfaces, forming boundary-driven fluctuations that stir the fluid around and generate globally directed flows and transport [1,2]. These accumulations are found across different length scales, from cytoskeletal elements at the cell cortex to microorganisms accumulating near fluid-fluid interfaces or close to rigid surfaces forming biofilms [3–11].

In such crowded and confined environments, transporting molecules, suspended particles, and fluids is crucial for maintaining continuous biological processes. These include clearing pathogens and self-cleaning, creating feeding currents, locomotion of reproductive cells, and cargo transport, which have direct implications for various fields, including microfluidics and life sciences [12–14].

The formation of these large quasi-two-dimensional boundary accumulations—referred to as *active carpets*—arises due to various stimuli, such as changes in viscosity or light in marine microorganisms, hydrodynamic interactions, mechanical responses, and optimization of metabolic activities [3,15–19]. Microbial swimmers are adapted to the inherently layered nature of aquatic environments, where physical, chemical, and biological properties undergo gradients in the direction of gravity. These layers result from abrupt changes in fluid properties, including temperature (thermocline), salinity (haloclines), dissolved oxygen (oxycline), dissolved chemicals (chemoclines), or sharp shifts in viscosity [4,20–25].

For example, natural thin slick layers of fluid–create abrupt changes in viscosity [26], promoting microbial accumulation and bloom formation [27,28]. Most of Earth's aquatic systems are capped by the air-water interface, known in oceans as the sea surface microlayer (SML). The SML, with a thickness ranging from 1 to 1000 micrometers, exhibits sudden changes in physical and chemical properties that sets it apart from the underlying waters [29–32]. This layering environment provides diverse niches for surface microbial swimmers (neuston) and inert suspended matter, both of which contribute to the marine biogeochemical pumping process [6,28,33,34]. In this context, vertical transport is essential for mixing and ventilation in thin, stratified environments.

A long-debated question is whether swimming organisms contribute to these processes in aquatic systems [35,36]. To

---

[*] Contact author: fbarros2017@udec.cl
[†] Contact author: ulloa@sas.upenn.edu
[‡] Contact author: g.aguayo07@gmail.com
[§] Contact author: amaths@sas.upenn.edu
[‖] Contact author: fguzman@uchile.cl

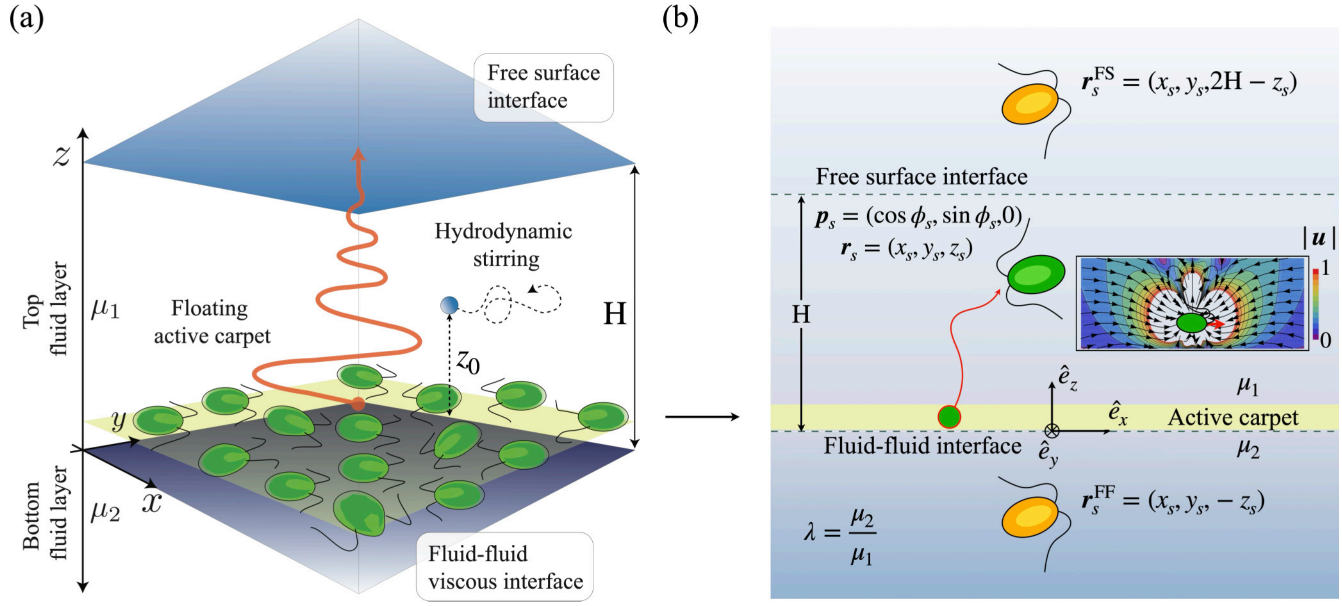

FIG. 1. (a) Schematic of a confined *active carpet* (yellow) between two fluid interfaces: the air-water interface at the top and a fluid-fluid interface at the bottom. The active carpet is composed of microswimmers located at a fixed distance σ above the bottom fluid-fluid interface (green). These microswimmers generate hydrodynamic fluctuations (orange arrows) which stir the fluid and suspended particles within the confined layer. (b) Conceptual model for a single microswimmer confined between the free surface (top) and the fluid-fluid interface (bottom). The microorganism swims in the x-y plane at $z = \sigma$ (green), creating two image swimmers (yellow) positioned at $\mathbf{r}_s^{\mathrm{FS}}$ and $\mathbf{r}_s^{\mathrm{FF}}$, respectively. Inset: The flow field generated in the x-z plane by a single puller-type microswimmer in a film of thickness $H = 3$, with $\kappa = -30$ and a viscosity ratio of $\lambda = 1.5$, computed from Eq. (9). Streamlines (black arrows) illustrate typical fluid parcel trajectories around the swimmer, and contours represent the velocity field's intensity, with higher intensity near the singularity (white) and lower intensity further away (purple).

investigate the flow field generated by a single microswimmer in a stratified environment, Ardekani and Stocker [37] employed the multipole expansion method, examining an organism moving at low Reynolds numbers ($\mathrm{Re} \ll 1$), where viscous forces dominate over inertial ones. Their results revealed that contractile swimmers in stratified fluids do not produce persistent flows conducive to vertical mixing. Instead, these swimmers generate in-plane flows that reinforce the existing stratification [37]. Theoretical studies support these findings, showing that at low Re, a single microbe swimming perpendicular to isopycnals, has minimal impact on mixing [38]. However, numerical and laboratory experiments have demonstrated that the collective vertical migration of small organisms—such as zooplankton swimming swimming at intermediate Reynolds numbers [$\mathrm{Re} \sim O(1)$] (e.g., Ref. [39])—can significantly enhance transport and mixing across fluid-fluid interfaces via hydrodynamic stirring [40–42].

Biogenic hydrodynamic stirring has been shown to enhance active diffusion [43–50], generate persistent flows for feeding processes in both collective and single microswimmers [1,9,51], induce aggregation [14,52–56], and trigger long-range hydrodynamic fluctuations in homogeneous fluid columns [57]. Recently, Aguayo *et al.* [53] studied the hydrodynamic fluctuations caused by *active carpets* formed by dipole microswimmers organized into a monolayer beneath the free surface of a semi-infinite homogeneous fluid. They found these fluctuations produce anisotropic diffusion, which decays slowly with distance, demonstrating a remarkable biogenic long-range effect on vertical transport. Additionally, artificial carpets composed of soft microswimmers, designed to mimic cilia and respond to magnetic, light, or electric stimuli, have drawn attention to their potential in fluid manipulation. These carpets, which can facilitate cargo delivery and fluid pumping, also provide a valuable experimental platform for studying the fundamentals of *active carpets* [58–62].

This paper focuses on *active carpets* living within a confined layer, bounded above by a free surface (the air-water interface) and below by a fluid-fluid interface characterized by a viscosity difference separating two fluid layers with viscosities μ_1 and μ_2, as illustrated in Fig. 1(a). Within this environment, an active carpet experiences two confining mechanisms: geometrical confinement, defined by the thickness of the upper layer H (the floating film), and viscous confinement, determined by the viscosity ratio $\lambda = \mu_2/\mu_1$. Here we investigate two scenarios for λ. In the first scenario, where $\lambda < 1$, the active carpet resides in a more viscous layer than the underlying fluid. In the second scenario, where $\lambda > 1$, the active carpet occupies a less viscous layer than the one below. Here λ provides insight into how soft ($\lambda \to 0$) or rigid ($\lambda \to \infty$) the fluid-fluid viscous interface behaves.

Our results differ significantly from previous studies on *active carpets*. Guzmán-Lastra *et al.* [57] explored active carpets near a no-slip surface, where the fluctuations decay as $\langle v_i^2 \rangle \propto z_0^{-4}$ for parallel dipoles. Similarly, Aguayo *et al.* [53] observed long-range fluctuations, with $\langle v_i^2 \rangle \propto z_0^{-2}$ near a free surface, where z_0 represents the vertical distance from the active carpet. In our study, however, the hydrodynamic fluctuations decay more intricately due to the confinement and influence of the viscous fluid-fluid interface. Although the anisotropic behavior of the variances persists, we found that the nature of the fluctuations can be controlled by the geometric and viscous microenvironment where the *active carpets* reside. Specifically, we demonstrate that at a critical distance $z_\star$ from the *active carpet*, the vertical fluctuations decay much more rapidly with z_0 than the horizontal fluctuations. This distinctive feature of the spatial structure of hydrodynamic fluctuations is examined in detail in the present paper.

The paper is structured as follows. In Sec. II, we introduce the mathematical model for a single swimmer moving at low-Re and active carpets in layered environments. We discuss the numerical modeling approach and parameters in Sec. III. In Sec. IV, we present and analyze our primary findings, which include new analytical solutions for active carpets in layered aquatic environments, analyses of the topology of hydrodynamic fluctuations, and the evidence of large-scale flow patterns driven by an *active carpet* in a tightly confined layered system. Our study sheds light on the complex interplay between confinement and hydrodynamics in these intriguing biological systems.

II. MATHEMATICAL MODEL

A. A microswimmer in a layered environment

We model the flow field of a single flagellated microswimmer moving in a homogeneous fluid of viscosity μ_1, confined between two nondeforming boundaries (e.g., Refs. [4,63]). The top boundary is a free surface, whereas the bottom is a fluid-fluid interface. Below this interface, there is a second fluid of viscosity μ_2, and the ratio between both fluid viscosities is denoted as $\lambda = \mu_2/\mu_1$. The distance between the top and bottom interface is H and is referred to as the film thickness, as depicted in Fig. 1(a).

Fluid motions induced by microscopic swimmers are characterized by the low-Reynolds-number regime, where viscous forces dominate the momentum balance [64,65]. Therefore, for a point force $\boldsymbol{F} = \boldsymbol{f}\delta(\boldsymbol{r}-\boldsymbol{r}_s)$ acting at position $\boldsymbol{r}_s = (x_s, y_s, z_s)$ on a stationary fluid of dynamic viscosity μ, fluid motions are governed by the incompressible Stokes equations [66],

$$\nabla p(\boldsymbol{r}) - \mu\nabla^2\boldsymbol{u}(\boldsymbol{r}) = \boldsymbol{F}, \tag{1a}$$

$$\nabla\cdot\boldsymbol{u}(\boldsymbol{r}) = 0, \tag{1b}$$

where $\boldsymbol{u}(\boldsymbol{r})$ and $p(\boldsymbol{r})$ are the fluid velocity and pressure field at position $\boldsymbol{r} = (x, y, z)$, respectively. In the absence of lateral boundaries, the solution of Eq. (1) is the well-known Stokeslet [67–69]

$$\boldsymbol{u}(\boldsymbol{r}, \boldsymbol{r}_s) = \frac{\mathcal{G}_{ij}(\boldsymbol{r}, \boldsymbol{r}_s)\cdot\boldsymbol{F}}{8\pi\mu}, \quad \mathcal{G}_{ij}(\boldsymbol{r}, \boldsymbol{r}_s) = \left(\frac{\delta_{ij}}{|\boldsymbol{d}|} + \frac{d_i d_j}{|\boldsymbol{d}|^3}\right), \tag{2}$$

where $\boldsymbol{d} = \boldsymbol{r} - \boldsymbol{r}_s$ is the relative position between the swimmer and the surrounding fluid. Derivatives of the Stokeslet are also solutions [70–72]. For swimming microorganisms, where the thrust and the drag force balance, the Stresslet is the first dominant term in the multipole expansion to describe their far-field flow [73].

Here, however, we must include the boundary conditions to fulfill the system's confinement. Following Desai and Ardekani [4], we construct the first approximation to the image system for the flow field produced by a microswimmer confined between the free surface and the fluid-fluid interface, as described in Fig. 1(b).

The Stokes equations for a point force acting on fluid 1 are

$$-\nabla p^{(1)} + \mu_1\nabla^2\boldsymbol{u}^{(1)} + \boldsymbol{F} = 0, \tag{3a}$$

$$\nabla\cdot\boldsymbol{u}^{(1)} = 0, \tag{3b}$$

while for fluid 2 they are

$$-\nabla p^{(2)} + \mu_2\nabla^2\boldsymbol{u}^{(2)} = 0, \tag{4a}$$

$$\nabla\cdot\boldsymbol{u}^{(2)} = 0. \tag{4b}$$

At the fluid-fluid interface, the velocity field of both fluids must satisfy the following boundary conditions [63]:

$$u_\alpha{}^{(1)} = u_\alpha{}^{(2)}, \quad \text{at} \quad z = 0 \tag{5a}$$

$$u_z^{(1)} = u_z^{(2)} = 0, \tag{5b}$$

$$\mu_1\left(\frac{\partial u_\alpha^{(1)}}{\partial z} + \frac{\partial u_z^{(1)}}{\partial \alpha}\right) = \mu_2\left(\frac{\partial u_\alpha^{(2)}}{\partial z} + \frac{\partial u_z^{(2)}}{\partial \alpha}\right) \quad \text{at} \quad z = 0, \tag{5c}$$

where $\alpha = x, y$. Likewise, at the free surface interface, the fluid 1 must satisfy the following boundary conditions:

$$u_z^{(1)} = 0, \quad \text{at} \quad z = H, \tag{6a}$$

$$\frac{\partial u_\alpha^{(1)}}{\partial z} + \frac{\partial u_z^{(1)}}{\partial \alpha} = 0, \quad \text{at} \quad z = H. \tag{6b}$$

From solving (3) to (5), the image's system for a point force between two fluids of different viscosities leads to a generalization of the Blake tensor [63]:

$$\begin{aligned}\mathcal{A}_{ij}(\boldsymbol{r}) = {}& \left(\frac{1-\lambda}{1+\lambda}\delta_{j\alpha}\delta_{\alpha k} - \delta_{j3}\delta_{3k}\right)\mathcal{G}_{ik}(\boldsymbol{r}) \\ & + \frac{2\lambda}{\lambda+1}h(\delta_{j\alpha}\delta_{\alpha k} - \delta_{j3}\delta_{3k})\frac{\partial}{\partial r_k}\left(\frac{h r_i}{r^3} + \mathcal{G}_{i3}(\boldsymbol{r})\right).\end{aligned} \tag{7}$$

Notice that for $\lambda = 0$, we recover the image flow field of a point force close to a free surface,

$$\mathcal{F}_{ij}(\boldsymbol{r}) = \mathcal{M}_{jk}\mathcal{G}_{ik}(\boldsymbol{r}), \tag{8}$$

where $\mathcal{M}_{jk}$ is a mirror matrix, $\mathcal{M} = \mathrm{diag}(1, 1, -1)$. This image system corresponds to the one satisfying the boundary conditions at $z = H$.

Formally, a point force $\boldsymbol{F} = \boldsymbol{f}\delta(\boldsymbol{r}-\boldsymbol{r}_s)$ is acting at position $\boldsymbol{r}_s = (x_s, y_s, z_s)$. The image system to account for the fluid-fluid interface is constructed using the propagator tensor in Eq. (7) for an image force located at position $\boldsymbol{r}_s^{\mathrm{FF}} = (x_s, y_s, -z_s)$, whereas for the free surface interface, we set a mirror image using Eq. (8) at position $\boldsymbol{r}_s^{\mathrm{FS}} = (x_s, y_s, 2H - z_s)$. The velocity field produced by a point force parallel to both interfaces is then given by

$$\begin{aligned}\boldsymbol{u}(\boldsymbol{r}, \boldsymbol{r}_s, \lambda, H) = {}& \mathcal{G}(\boldsymbol{r}, \boldsymbol{r}_s)\cdot\boldsymbol{f}_\parallel + \big(\mathcal{F}(\boldsymbol{r}, \boldsymbol{r}_s^{\mathrm{FS}}, H) \\ & + \mathcal{A}(\boldsymbol{r}, \boldsymbol{r}_s^{\mathrm{FF}}, \lambda)\big)\cdot\boldsymbol{f}_\parallel,\end{aligned}$$

where the second term is the full image system added to satisfy the induced hydrodynamic boundary conditions and $\boldsymbol{f}_{\parallel} = \boldsymbol{f}/(8\pi\mu_1)$ is the scaled force.

We can then measure the velocity field of a force dipole with orientation $\boldsymbol{p}_s$ as shown in Fig. 1(b),

$$\boldsymbol{u}_D(\boldsymbol{r}, \boldsymbol{r}_s, \boldsymbol{p}_s) = \kappa\,(\boldsymbol{p}_s \cdot \boldsymbol{\nabla}_s)[(\mathcal{G} + \mathcal{F} + \mathcal{A}) \cdot \boldsymbol{p}_s]. \tag{9}$$

Here derivatives $\boldsymbol{\nabla}_s = \partial/\partial \boldsymbol{r}_s$ are taken with respect to the microswimmer's position. The coefficient $\kappa = f_{\parallel}\sigma$ corresponds to the dipolar strength, which characterizes the hydrodynamic distortions of each microswimmer and sets the timescale of the driven flow, $\tau = \sigma^3/\kappa$, with σ the microswimmer body length. On the one hand, when $\kappa > 0$, the microswimmer generates an extensile flow (pusher) similar to motile bacteria powered by a helical flagella bundle. On the other hand, when $\kappa < 0$, the flow field is contractile (puller) similar to the flow generated by green microalgae *Chlamydomonas reinhardtii* [74], as shown in the inset of Fig. 1(b).

In this study, we utilize the leading-order image system to describe the far-field flow of a dipole microswimmer [4]. It is important to note that boundary conditions are only partially satisfied when two image flow fields are added to the hydrodynamic system. To mitigate this discrepancy, recursive images of the original images must be added. However, since the first images closely approximate the confined natural system under investigation, they encapsulate most of the relevant physics. Therefore, for simplicity, we neglect the higher-order image solutions [9].

In nature, sharp vertical temperature gradients, the sea surface microlayer or the presence of natural and artificial slicks can lead to abrupt changes in fluid viscosity, especially at the skin of surface waters [28,31,75]. Also, during blooms, planktonic microorganisms have been reported to increase the effective ambient viscosity, generating strong viscosity gradients with relative viscosities $1 \lesssim \lambda \lesssim 3$ at short distances [16]. Microorganisms in mammals' guts and tracts also swim in regions of high viscosity contrast or mucus, with some bacteria performing positive viscotaxis and some other strains performing negative viscotaxis among these regions [76–78]. Recent research has studied the microorganisms' optimal swimming behavior in viscosity gradients (viscotaxis), revealing divergent trends. In some cases, microorganisms prefer swimming in low-viscosity regions, while in others, they favor high-viscosity environments [15,76,79–81]. For instance, the *C. reinhardtii*, a type of phytoplankton, shows viscophobic behavior by accumulating in the region of lower viscosity $\lambda > 1$ [17].

In recent experiments, bacterial baths within microdroplets of water in oil ($\lambda < 1$) have been studied with different bacterial strains. In the case of magnetotactic bacteria, it was observed that they drive a vortex flow in the center of the microdroplet in the presence of strong external magnetic fields [25]; this was also corroborated with numerical simulations showing a fragile equilibrium between high bacterial concentrations, activity, confinement, and taxis [24]. In the case of a suspension of *Escherichia coli*, the bacterial bath generates hydrodynamic fluctuations that self-propel the microdroplet [82], or in the case of a double emulsion, the suspended particle at the core of the microdroplet is inherent to the microscopic parameters of the bacterial suspension, such as memory time and length scales [83].

B. *Active carpet* in a layered aquatic environment

It has been observed that microorganisms concentrate near fluid interfaces, where they swim in a partially tilted orientation with respect to the interface [6,84]. Their spatial distribution is well represented by an exponential function that peaks near the interface and decays along the vertical direction [85]. Here we approximate this distribution by assuming that all microorganisms reside in a two-dimensional horizontal plane. Thus, our model considers a collection of dipole microswimmers forming the so-called *active carpet*, confined to swim in the x-y plane at a fixed height $z_s = \sigma$ above the viscosity interface, as sketched in Fig. 1(a). We show that although this model simplifies real-world scenarios, it qualitatively and quantitatively reproduces the fluctuations generated by thicker carpets (see Secs. I and II in Supplemental Material [86]). This was recently confirmed for an *active carpet* near a free interface [53].

A similar result is observed when considering that not all microorganisms align perfectly parallel to the interface. We refer the reader to Sec. III in Supplemental Material [86] for the cases of a tilted carpet and a thick tilted carpet. In both scenarios, we recover results similar to those for microorganisms swimming parallel to the fluid interface, which is the focus of this study.

Our *active carpet* consists of a dense suspension of microorganisms, each residing at positions $\boldsymbol{r}_s = (x_s, y_s, \sigma)$ and having orientations $\boldsymbol{p}_s = (p_x, p_y, 0)$. We consider a stroboscopic diffusive regime [53,57], where microswimmers are uniformly distributed in both space and orientation on a two-dimensional surface over time. Each microorganism stirs the confined water film, generating a flow field described by Eq. (9). We analyze the biogenically driven flow at positions $\boldsymbol{r}_0 = (x_0, y_0, z_0)$, corresponding to a fluid parcel between the free surface and the fluid-fluid interface. To derive a far-field approximation for the collective flow driven by the *active carpet*, we perform a Taylor expansion of the flow field generated by a single microswimmer, assuming $z_s = \epsilon z_0$ with $\epsilon \ll 1$ (see details in the Supplemental Material [86]). The resulting analytical expression enables us to calculate various statistical properties of the collective flow.

The mean flow field averaged over a finite carpet of size R with microswimmer uniformly distributed in cylindrical coordinates ρ_s and θ_s and orientations ϕ_s is

$$\langle \boldsymbol{v}(\boldsymbol{r}) \rangle = \int \boldsymbol{u}(\boldsymbol{r}, \boldsymbol{r}_s, \boldsymbol{p}_s)\, \mathcal{F}(\boldsymbol{r}_s, \boldsymbol{p}_s)\, d\boldsymbol{r}_s d\boldsymbol{p}_s, \tag{10}$$

where $\mathcal{F} = n/2\pi > 0$ is a uniform distribution of swimmers for a carpet number density n and $\langle\cdot\rangle$ denotes the average over the collection of swimmers. Here $\boldsymbol{r_s} = (\rho_s \cos\theta_s, \rho_s \sin\theta_s, \sigma)$ is the swimmer's position and $\boldsymbol{p_s} = (\cos\phi_s, \sin\phi_s, 0)$ the swimmer's orientation, with $\phi_s, \theta_s \in [-\pi, \pi]$. Notably, a finite carpet can generate drift, as observed when microorganisms swim near a no-slip boundary [2]. However, this drift diminishes as the *active carpet* size increases, i.e., $R \to \infty$ [57]. For consistency, we consider an infinite carpet, where $\langle \boldsymbol{v}(\boldsymbol{r}) \rangle = 0$ and the variance $\mathcal{V}ij = \langle \boldsymbol{v}_i \boldsymbol{v} j \rangle$ is nonzero. Here

$i, j = x, y, z$ represent the Cartesian components of the flow. The variance, which represents the fluctuations, governs the active diffusion experienced by tracer particles above the carpet. The geometry of the system strongly influences its magnitude and can be computed analytically using the following expression for the variance tensor:

$$\mathcal{V}_{ij} = \langle v_i v_j \rangle = \int u_i u_j \mathcal{F}\, d\boldsymbol{r}_s d\boldsymbol{p}_s. \tag{11}$$

Additionally, we define the average vorticity field induced by the confined *active carpet* as:

$$\langle \boldsymbol{\omega} \rangle = \langle \nabla \times \boldsymbol{v} \rangle = \int (\nabla \times \boldsymbol{u}) \mathcal{F}\, d\boldsymbol{r}_s d\boldsymbol{p}_s, \tag{12}$$

and the average circulation over an area S as:

$$\Gamma = \iint_S \langle \boldsymbol{\omega} \rangle \cdot d\mathbf{S}. \tag{13}$$

We now turn the focus to the numerical framework utilized to simulate the dynamics of confined *active carpet*.

III. NUMERICAL SIMULATIONS

As discussed in Sec. II B, we do not follow each microswimmer's trajectory in time. Instead, we investigate the fluctuations induced by the *active carpet* in the surrounding fluid after the microswimmers transition from the ballistic regime to a diffusive regime (e.g., Refs. [53,57]).

In summary, we model *active carpets* through the fast dynamics framework. The fast dynamics framework is made by randomly distributing $N_s = 10^5$ microswimmers with uniformly distributed positions $\boldsymbol{r}_s = (x_i, y_i, \sigma)$ and orientations $\boldsymbol{p}_s = (\cos\phi_i, \sin\phi_i, 0)$, with $\phi_i \in [-\pi, \pi]$, $i \in [1, N_s]$ in a finite square domain, $2L \times 2L$, where $2L$ is the size of the *active carpet*. The microswimmers number density in the *active carpet* is defined as $n = N_s/(2L)^2$.

The total flow generated by the *active carpet* is computed by superimposing the flow velocity of each individual microswimmer, as given by Eq. (9). Therefore, the collective velocity field driven by the ensemble is determined by:

$$\boldsymbol{v}(\boldsymbol{r}, \boldsymbol{r}_s, \boldsymbol{p}_s) = \sum_{i=1}^{N_s} \boldsymbol{u}_D(\boldsymbol{r}, \boldsymbol{r}_s, \boldsymbol{p}_s). \tag{14}$$

This velocity is computed for an ensemble of N_e-independent *active carpet* configurations.

Hence, we compute the variance tensor of the flow field Eq. (14) as defined in Eq. (11), averaging over a finite number of *active carpet* ensembles N_e. Using this framework, we investigate the dynamics of passive tracer particles stirred by the collective action of the microswimmers colony. A tracer particle, with position $\boldsymbol{r}^T(t)$, evolves following the motion equation:

$$\frac{d\boldsymbol{r}^T(t)}{dt} = \boldsymbol{v}(\boldsymbol{r}^T, \boldsymbol{r}_s, \boldsymbol{p}_s). \tag{15}$$

As illustrated in Fig. 1(a), we explore tracer particle dynamics between the *active carpet* and the free surface with $\sigma < z_0 < H$. We integrate Eq. (15) numerically utilizing a Euler scheme, with a nondimensional integration time step $\Delta t = 3 \times 10^{-2}\tau$. At each time step, the tracer particle excursions a length $\Delta \boldsymbol{r}^T$ determined by a new random independent *active carpet* ensemble.

In this study, unless otherwise specified, we use the following parameters: microswimmer body length and length scale $\sigma = 1$, the dipole strength $\kappa = f_\parallel \sigma = -30$ for a puller and $\kappa = 30$ for a pusher following [74,87], number density $n = 0.1$, microswimmers's number $N_s = 10^5$, film thickness small parameter $\epsilon = 0.1$, ensemble number $N_e = 10^3$, and *active carpet* total length $2L = 10^3$. Our primary focus is investigating the impact of the confinement size H and the interface strength λ. In the following, we explore how the degree of fluid confinement impacts the spatial characteristics of the hydrodynamic stirring driven by *active carpets*.

IV. RESULTS AND DISCUSSION

A. Fluctuation and dispersion of tracer particles

We first characterize the hydrodynamic fluctuations driven by the confined *active carpet* whose members swim parallel to the fluid-fluid interface, as sketched in Fig. 1(a). According to the theory developed by Mathijssen *et al.* [2], we can directly compute the variance of the flow field (11) by performing a far-field approximation of the flow field (Sec. II B). It is important to note that the off-diagonal components of the variance tensor vanish. Additionally, due to symmetry, we have $\langle v_x^2 \rangle = \langle v_y^2 \rangle$ [57]. Therefore, we only need to characterize two components of the fluctuations: the horizontal component $\langle v_x^2 \rangle$ and the vertical component $\langle v_z^2 \rangle$.

As a consequence of the confined geometry and the boundary conditions, the velocity field and its variance depend on the ratio $\lambda = \mu_2/\mu_1$, characterizing the viscous interface, the thickness of the aquatic film H, as well as the intrinsic physical and geometrical parameters of the Stokes solution and far-field approximation. Hence, each variance component is a function of $\langle v_i^2 \rangle = \langle v_i^2 \rangle(n, \kappa, \sigma, \lambda, \epsilon, H, z_0)$, where z_0 is the height of a fluid parcel relative to the *active carpet*. The obtained analytical expressions are

$$\begin{aligned}\langle v_x^2 \rangle = \frac{\pi\kappa^2 n}{64}\Bigg(&\frac{21\sigma^2\epsilon^2 - 22\sigma\epsilon(z_0 - 2H) + 11(z_0 - 2H)^2}{(z_0 - 2H)^4} + \frac{336\sigma^2\lambda^2\epsilon^2}{(\lambda+1)^2 z_0^4} + \frac{160\sigma\lambda\epsilon}{(\lambda+1)^2 z_0^3}\\ &+ \frac{36 z_0(8\sigma\lambda\epsilon(H + 2\sigma\epsilon) + H(2H + 3\sigma\epsilon))}{H^5(\lambda+1)} - \frac{36 z_0^2(2\sigma\lambda\epsilon(2H + 5\sigma\epsilon) + H(H + 2\sigma\epsilon))}{H^6(\lambda+1)}\\ &+ \frac{8H(H + \sigma\epsilon) - 32\sigma\lambda\epsilon(2H + 3\sigma\epsilon)}{H^4(\lambda+1)} + \frac{44}{(\lambda+1)^2 z_0^2}\Bigg),\end{aligned} \tag{16a}$$

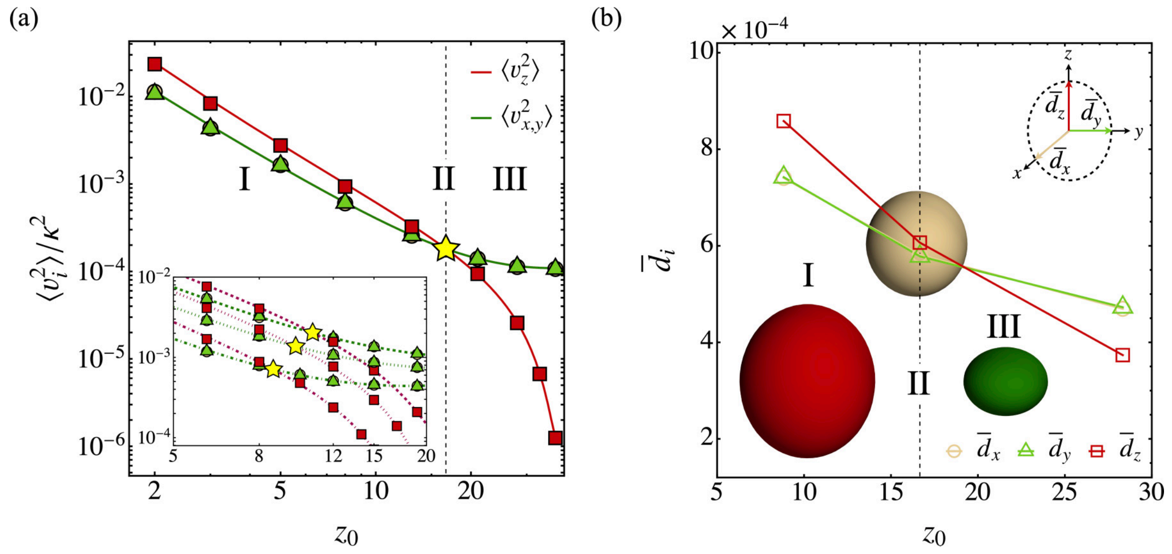

FIG. 2. Anisotropic hydrodynamic fluctuation driven by *active carpets*. (a) Variance of the flow field driven by an *active carpet* in the horizontal and vertical directions (green and red solid lines), as defined in Eq. (11). Markers are simulation points obtained from Eq. (14). The star marks the intersection between theoretical variances $\langle v_z^2\rangle(z_\star) = \langle v_{xy}^2\rangle(z_\star)$. Regions I, II, and III indicate the dominance of fluctuations according to the distance from the active carpet. Here $H = 40$ and $\lambda = 1.5$. Inset: Theoretical variances for $H = 20$, and three different values of λ, $\lambda = 0.1, 0.5, 1.5$, denoted by dashed, dotted, and dash-dotted lines, respectively. Stars are cross-points. (b) Ellipsoids represent the average displacement of tracer particles computed from Eq. (15) for each fluctuation region. In green, tracer particles start at $z_0 < z_\star$, while in red, they start at $z_0 < z_\star < H$. In ginger, they start exactly at $z_0 = z_\star$.

$$\langle v_z^2\rangle = \frac{9\pi\kappa^2 n}{32}\left(\frac{2\sigma^2\epsilon^2 - 2\sigma\epsilon(z_0-2H) + (z_0-2H)^2}{(z_0-2H)^4} + \frac{80\sigma^2\lambda^2\epsilon^2}{(\lambda+1)^2 z_0^4} + \frac{32\sigma\lambda\epsilon}{(\lambda+1)^2 z_0^3}\right.$$
$$\left. - \frac{4z_0(8\sigma\lambda\epsilon(H+2\sigma\epsilon) + H(2H+3\sigma\epsilon))}{H^5(\lambda+1)} + \frac{4z_0^2(2\sigma\lambda\epsilon(2H+5\sigma\epsilon) + H(H+2\sigma\epsilon))}{H^6(\lambda+1)} + \frac{4}{(\lambda+1)^2 z_0^2}\right). \tag{16b}$$

Note that the hydrodynamic fluctuations driven by the active carpet are proportional to the number density n and the square of the dipole strength κ^2. Consequently, the behavior of these fluctuations remains independent of whether the swimmer acts as a puller or a pusher. Additionally, while $\epsilon \ll 1$ it is not zero, the limit $\epsilon \to 0$ does not have a physical interpretation.

To validate these analytical results, we performed simulations using Eq. (14), numerically obtaining the variance for various values of z_0 within the range (σ, H). We set the body length σ as the unit of length throughout our results.

Figure 2(a) presents both the analytical and simulation results for the variance with $\lambda = 1.5$ and $H = 40$. The agreement between theory and simulations is excellent. The effect of confinement on the biogenically driven fluctuations is severe: the horizontal and vertical fluctuations are anisotropic ($v_z^2 \neq v_x^2$) and both vary differently with z_0. Moreover, they intersect at a specific location denoted as $z_0 = z_\star$. For the current parameters, this occurs at $z_\star = 16.6 = 0.43H$ (indicated by the yellow star in the plot). For smaller z_0 values, the vertical variance is larger than the horizontal one and vice versa. This crossover can also be predicted using Eqs. (16a) and (16b), noting that $z_\star$ depends on H and λ.

Therefore, we define three distinct regions: Region I (vertical fluctuations dominate), Region II (fluctuations are isotropic); and Region III (horizontal fluctuations dominate). To illustrate this feature, the inset shows the fluctuation behavior for different values of λ ([0.1,0.5,1.5] in dashed, dotted, and dot-dash, respectively) and film thickness $H = 20$. The variance curves intersect similarly, and the crossover point $z_\star$ shifts depending on the value of λ—lower values move the intersection closer to the free surface, while higher values shift it toward the *active carpet*. In summary, characterizing the locus $z_\star$ and its dependence on the parameters is crucial because it indicates where the fluctuations and flow direction become spatially biased.

To validate the anisotropic behavior of fluctuations and its effect on tracer particles, we carried out simulations using Eq. (15) with an *active carpet* confined within a film of thickness $H = 40$ and viscosity ratio $\lambda = 1.5$. From the analytical solution (16), we calculated the intersection height $z_\star$ by solving $\langle v_x^2\rangle(z_\star) = \langle v_z^2\rangle(z_\star)$. We then seeded passive tracers at different heights relative to $z_\star$ to explore their dynamics in each region. Particles were released at heights $z_0 = 27.7 > z_\star$, $z_0 = z_\star$, and $z_0 = 10 < z_\star$ to measure vertical-dominated, isotropic, and horizontal-dominated motions, respectively.

Simulating for $\tau_e = 180$ time steps allowed us to characterize the spatial topology of tracer transport, based on the average displacement $\bar{d}_i$ for each direction $\hat{e}_i$ (with $i = x, y, z$). The ellipsoids in Fig. 2(b) (scaled for visualization) show

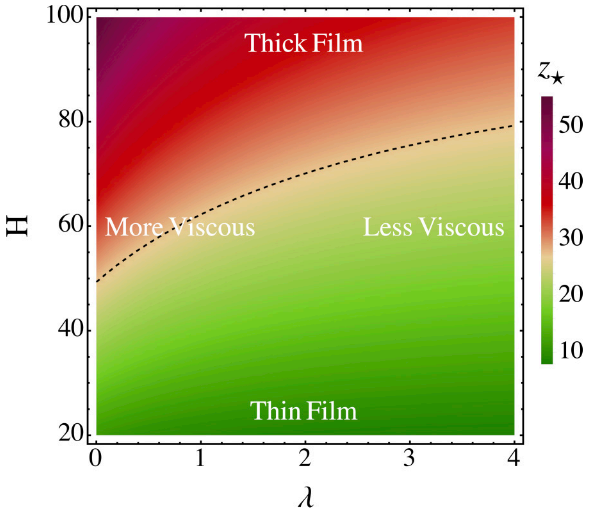

FIG. 3. The impact of confinement on the localization of $z_\star$. Analytical solutions for the cross-point height $z_\star$ for a domain of the parameters λ and H. We described the domain showing the cases of thicker and thinner films and for more and less viscous films, where $\lambda = \mu_2/\mu_1$ with μ_1 the fluid viscosity where the AC resides.

the resulting topology for each region. Thus, we confirm that tracer particles have a more prominent vertical motion at heights $z_0 < z_\star$ (red) closer to the *active carpet*, equal to horizontal motions at $z_0 = z_\star$ (ginger) and that horizontal motions become dominant at $z_0 > z_\star$ (green).

In general, the transport capacity of a system can be characterized by measuring the enhanced diffusion on tracer particles compared to Brownian motion. This enhancement can be quantified through the hydrodynamic fluctuations driven by the active carpets [52,53]. Section IV of the Supplemental Material [86] provides a brief description of the enhanced diffusion of the system investigated here.

B. Impact of confinement on fluctuation's geometry

In the previous section, we demonstrated the zonification of hydrodynamic fluctuations across the fluid layer. Now, we explore how the degree of confinement, determined by H and λ, impacts the spatial distribution of these fluctuations. Here we specifically address the variation of $z_\star$ with respect to λ and H. Figure 2 illustrates the significant anisotropic behavior of the fluctuations induced by the confined *active carpet*. A key result is the existence of three distinct regions, whose boundaries are determined by $z_\star$, the height where the vertical and horizontal variances of the velocity fluctuations are equal. Below $z_\star$, vertical fluctuations dominate, while above $z_\star$, horizontal fluctuations dominate. The analytical solution (16) reported in Sec. IV A enables us to describe how these regions vary as functions of H and λ.

To compute $z_\star(\lambda, H)$, we solved the nonlinear equation $\langle v_x^2\rangle(z, H, \lambda) - \langle v_z^2\rangle(z, H, \lambda) = 0$ for $z \in (\sigma, H)$, where the root corresponds to $z_\star$. Figure 3 shows the dependency of $z_\star$ on H and λ over the range $\lambda \in [0, 4]$ and $20 \leqslant H \leqslant 100$. First, we observe that $z_\star$ increases monotonically with H. This implies that thicker aquatic films create conditions where vertical fluctuations dominate over horizontal fluctuations. From an ecological viewpoint, this is relevant since the *active carpet* can have a longer range for attracting or repealing mass. Second, $z_\star$ is larger for smaller λ. In other words, the more viscous the layer where the *active carpet* habits, the longer the extent of the region where vertical fluctuations dominate over horizontal fluctuations.

In the extreme case of $\lambda \to 0$, the fluid surrounding the *active carpet* is significantly more viscous than the fluid beneath it, characterized by $\mu_1 \gg \mu_2$. Such substantial viscosity differences can occur in both freshwater and marine environments, especially during algae blooms, which can locally alter the physicochemical properties of the water column. While these variations may push the fluid away from a strictly Newtonian behavior, Newtonian rheology remains a reasonable approximation for fluids with gently varying viscosities, as is often the case with liquid water [88,89].

For $\lambda = 0$, and the range of H values we examine, we find that $z_\star = 0.55H$. In contrast, when $\lambda = 0.5$, we obtain that $z_\star = H/2$, indicating that fluctuations in regions I and III are nearly equivalent in extent. As λ increases, this proportionality changes.

Figure 3 shows a different result for $\lambda = 4$, where we find that in average $z_\star = 0.35H$. In this scenario, the fluid-fluid interface strengthens by making λ larger. Consequently, from our framework, one would expect to recover the well-studied hydrodynamic system of a free-surface liquid film held by a rigid surface for $\lambda \gg 1$ [9]. As a result, we observe that for larger λ, the hydrodynamic fluctuations are, on average, more planar-directed motions than vertical motions since the region dominated by vertical fluctuations reduces to 35% of the film's thickness, i.e., horizontal fluctuations dominate over 75% of the film.

This behavior mirrors the viscous control observed in analogous scenarios, such as superconfined subsurface faults, where viscosity drives fluid flow fluctuations towards quasi-two-dimensional states [90]. From these results, it is apparent that λ plays a significant role in unbalancing the system and changing the architecture of the hydrodynamic fluctuations so that the confined *active carpet* may promote, for example, biogenic mass reorganization mechanisms such as aggregation, recently investigated in a semi-infinite fluid [53].

C. Circulation and roll-like formation

The results in Fig. 3 underscore the influence of geometrical and viscous confinements on the spatial structure of velocity fluctuations. Beyond affecting fluctuations, this confinement also exerts control over passive tracer trajectories. This raises an intriguing question: Could confined *active carpets* catalyze the emergence of large-scale coherent flow patterns? To explore this, we examine the coherence of fluid motions using pair velocity correlation and vorticity fields.

A defining feature of living systems is their ability to generate mechanical disturbances over scales greater than their individual size, which is key for enhancing mixing in aquatic environments. The ability of swimming organisms to stir fluids through interactions has been well-established [40,41,45,47,48,50,91]. While individual swimmers in stratified waters have limited mixing capabilities [3,38], whether collective action can significantly impact

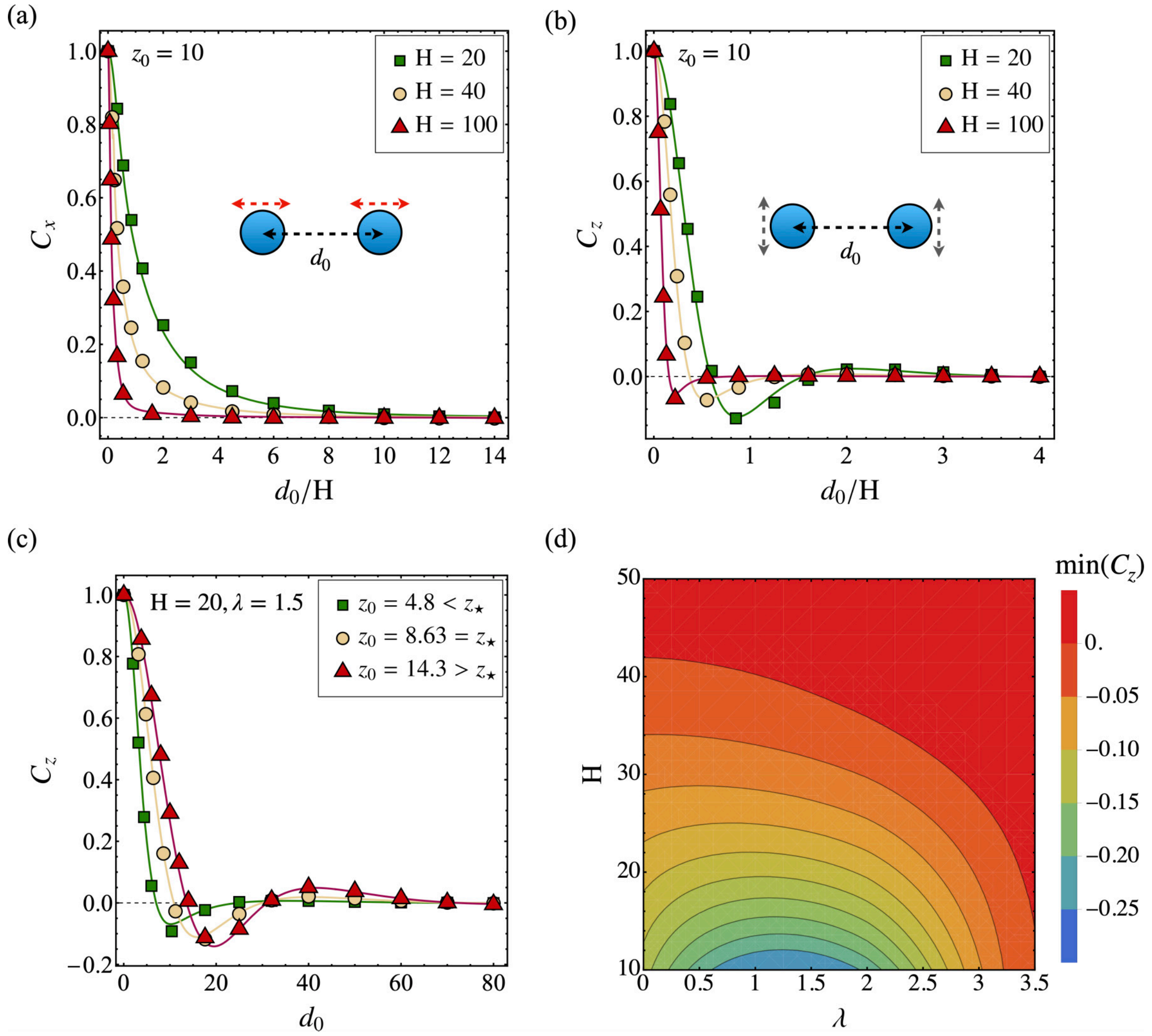

FIG. 4. [(a) and (b)] Velocity pair correlation function $C_x(d_0)$, $C_z(d_0)$ in terms of the relative distance between a pair of tracer particles, d_0, normalized by the confinement size relative to the active carpet H measured at height $z_0 = 10$, for pullers microswimmers with $\lambda = 1.5$, $\sigma = 1$, and $\kappa = -30$. Plot markers correspond to numerical simulations using Eq. (17) and lines to the semianalytical far-field approximation using Eq. (10). Insets: Illustrative scheme for measuring the velocity pair correlation between two fluid parcels separated by a distance d_0. (c) Vertical velocity pair correlation function $C_z(d_0)$, for $H = 20$ and $\lambda = 1.5$ at different heights z_0 according to fluctuations regions described in Sec. IV B. (d) Phase diagram of the vertical pair correlation minima, measured at $z_0 = 10$, as a function of λ and H.

the fluid environment remains under debate [35,36,38]. This motivates our study of large-scale hydrodynamic structures induced by *active carpets* in confined aquatic systems. Pair velocity correlation emerges as a useful metric for understanding these relationships [2,52,53].

We compute the spatial pair velocity correlation to examine how geometrical and viscous confinement affects flow coherence, defined as

$$C_i(d_0) = \frac{\langle v_i(\boldsymbol{r}_1)v_i(\boldsymbol{r}_2)\rangle_e}{\sqrt{\left\langle v_i^2(\boldsymbol{r}_1)\right\rangle_e \left\langle v_i^2(\boldsymbol{r}_2)\right\rangle_e}}, \qquad (17)$$

where $d_0 = |\boldsymbol{r}_2 - \boldsymbol{r}_1|$ is the Euclidean distance between two fluid parcels in position $\boldsymbol{r}_1$ and $\boldsymbol{r}_2$ with fixed height z_0, above the *active carpet*. The operator $\langle\cdot\rangle_e$ represents an *active carpet* ensemble average, and the variance tensor (11) is utilized to compute the numerator in Eq. (17). To calculate Eq. (17) from numerical simulations, we first evaluate the flow induced by the *active carpet* at $\boldsymbol{r}_{1,2} = (\pm d_0/\sqrt{2}, \pm d_0/\sqrt{2}, z_0)$ with $z_0 = 10$ for a wide range of distances d_0. Then we compute Eq. (17) for each ensemble and take the average over ensembles. Results are shown and discussed next.

Figure 4(a) displays the pair velocity correlation, $C_x(d_0)$, in the $\hat{e}_x$ direction, representing horizontal correlation, as a function of d_0/H for pullers microswimmers. For simplicity, we omit results for $\hat{e}_y$, which is symmetric to those in $\hat{e}_x$. We examine the horizontal velocity pair correlation between particles separated by a distance d_0 (see insets) for three H values ($H \in [20, 40, 100]$), with a fixed $\lambda = 1.5$ and a representative height $z_0 = 10$ above the active carpet. Note that we normalize d_0 by H to gauge the characteristic length of decorrelation relative to the film thickness.

The varying H range allows us to observe that increasing geometrical confinement (i.e., thinner H) expands the relative extent of positively correlated tracer motions over distance d_0, indicating that horizontal flows decorrelate more slowly in confined systems. Our numerical results align with semianalytical solutions $\langle v_i(\boldsymbol{r}_1)v_i(\boldsymbol{r}_2)\rangle = \int v_i(\boldsymbol{r}_1)v_i(\boldsymbol{r}_2)F d\boldsymbol{r}_s d\boldsymbol{p}_s$, shown by solid lines in Fig. 4.

Given that the confinement of *active carpets* primarily occurs in the vertical direction, we examine the horizontal pair correlation in the $\hat{e}_z$ direction, $C_z(d_0)$, which we refer to as vertical pair correlation. The results in Fig. 4(b) for $\lambda = 1.5$ demonstrate not only good agreement between numerically obtained results (markers) and semianalytical solutions (lines) but also reveal notable differences from horizontal pair correlation (C_x), as shown in Fig. 4(a).

In contrast, the vertical pair correlation, $C_z(d_0)$, as shown in Fig. 4(b), decays more rapidly than the horizontal correlations and reaches a minimum for $d_0 \approx H$. This indicates that fluid parcels are moving in opposite directions at distances that scale with the confinement size. This behavior suggests the formation of coherent flow structures in highly confined environments, which has also been observed in microswimmer's sheets, active turbulence experiments, and bacterial swarming [92–94].

In Sec. IV A, we defined the region where active fluctuations show a preferred direction. This effect is caused by the flow, so we thoroughly examined the vertical pair correlation C_z. To illustrate how C_z changes at different heights, we kept the values of $H = 40$ and $\lambda = 1.5$ fixed while varying the position z_0 at which flows are measured. The results shown in Fig. 4(c) demonstrate how sensitive C_z is to the height above the active carpet.

To further explore the intensity of this negative correlation, we vary H and λ. Figure 4(d) presents the minimum vertical pair correlation $\min(C_z)$ for film thickness in the range $H \in [10, 50]$ and viscosity ratio $\lambda \in [0, 3.5]$, computed using the semianalytical approach at a fixed distance $z_0 = 10$. Our analysis reveals that the negative correlation, and thus the intensity of opposing flows, becomes larger with increased geometrical confinement. We also observe that viscous confinement, controlled by λ, enhances the negative correlation $\min(C_z)$ within the range $\lambda \in [0.5, 2]$. This interesting dependence with λ is warrants future research for extreme conditions [4].

The question of whether confined fluid environments give rise to large-scale flow structures remains open. In this study, we explore the emergence of vortical flows induced by confined *active carpets* by analyzing the spatial structure of flow vorticity Eq. (12) and circulation Eq. (13). These quantities are studied within a Cartesian coordinate system (x, y, z) to guide our search for large-scale patterns amidst biogenic flow fluctuations. Figures 5(a)–5(c) illustrates the vorticity field for puller microswimmers on the z-x plane (over a finite region of size $2H \times H$) for $H = 20$, $\lambda = 1.5$, and $\kappa = -30$, calculated using a semianalytical approach with a spatial resolution of $\Delta z = 0.5$ and $\Delta x = 0.5$. We visualize coherent trends by highlighting the vortical velocity component ω_j, with counterclockwise motions in red (+1), clockwise motions in blue (−1), and no motion in white (0). These results confirm the presence of vortical flow patterns, resembling roll-like formations characterized by alternating regions of positive and negative vorticity, particularly evident in the case of the vorticity component ω_y which is normal to the x-z plane as shown in Fig. 5(b). To emphasize this point, we illustrate the direction of vorticity with arrows at the top of the figure and display the vertical velocity component v_z [see Fig. 5(d)] in the same plane. This reveals a strong downwelling flow in the central region, flanked by areas of upwelling on either side.

To further support these findings, we calculated the circulation $\Gamma(\ell)$ over squared surfaces ℓ^2 for vorticity ω_y normal to the x-z plane. Figures 5(d) and 5(e) define three regions (A, B, and C) where we measured circulation over different squared areas, observing circulation in opposite directions in regions A (blue) and B (red). These opposing vortical flows, with varying sizes ℓ, were compared with the system size H. Additional results for pushers on the z-y plane with $H = 16$, $\lambda = 0.25$, and $\kappa = 30$ (Figs. 3 and 4 in the Supplemental Material [86]) confirm that the emergence of vortical flows is not dependent on the type of microswimmer, though confinement enhances these structures.

Our findings demonstrate the potential of *active carpets* to drive large-scale flow structures in confined environments, bearing similarities to phenomena like bioconvection [23,45], biogenic flows in confined systems [94], thermally driven convection [95,96], and even culinary-inspired flows [97]. These results open fundamental questions about the role of *active carpets* inhabiting layered environments to shape their surroundings, enhance the mixing of suspended and dissolved mass in aquatic environments, and facilitate transport between fluid-fluid interfaces and layers.

V. CONCLUSIONS

We have explored the hydrodynamics of confined *active carpets* in layered aquatic systems, focusing on three main aspects: (i) characterizing the spatial distribution of hydrodynamic fluctuations and the dispersion of passive tracers (Sec. IV A), (ii) assessing the influence of geometrical and viscous confinement on *active carpets*–induced hydrodynamics (Sec. IV B), and (iii) the emergence of large-scale hydrodynamic structures, termed roll-like formations (Sec. IV C).

Our main findings are as follows:

(1) We derived and reported analytical expressions for the active flow fluctuations generated by *active carpets* confined within a layer of thickness H, situated between a free surface and a fluid-fluid interface defined by a viscosity ratio λ. The solutions reveal a crossover in the anisotropic behavior of the fluctuations, where the relative importance of the vertical and the horizontal fluctuations is space dependent. This differs completely from observations made in *active carpets* near a single surface system [53,57]. These biogenic fluctuations are intricately controlled by the degree of geometrical and viscous confinement characterized by H and the viscosity ratio $\lambda = \mu_2/\mu_1$, where μ_1 is the viscosity of the fluid where the *active carpet* resides, and μ_2 represents the viscosity of the deeper layer. Numerical simulations confirm the analytical findings and provide deeper insights into the dynamics of passive tracer particles, highlighting the height-dependent topology of motions above the *active carpet*.

(2) We showed that the topology of hydrodynamic fluctuations transforms according to the degree of geometrical confinement and the intensity of the viscosity ratio at the fluid-fluid interface boundary. Notably, we identified three

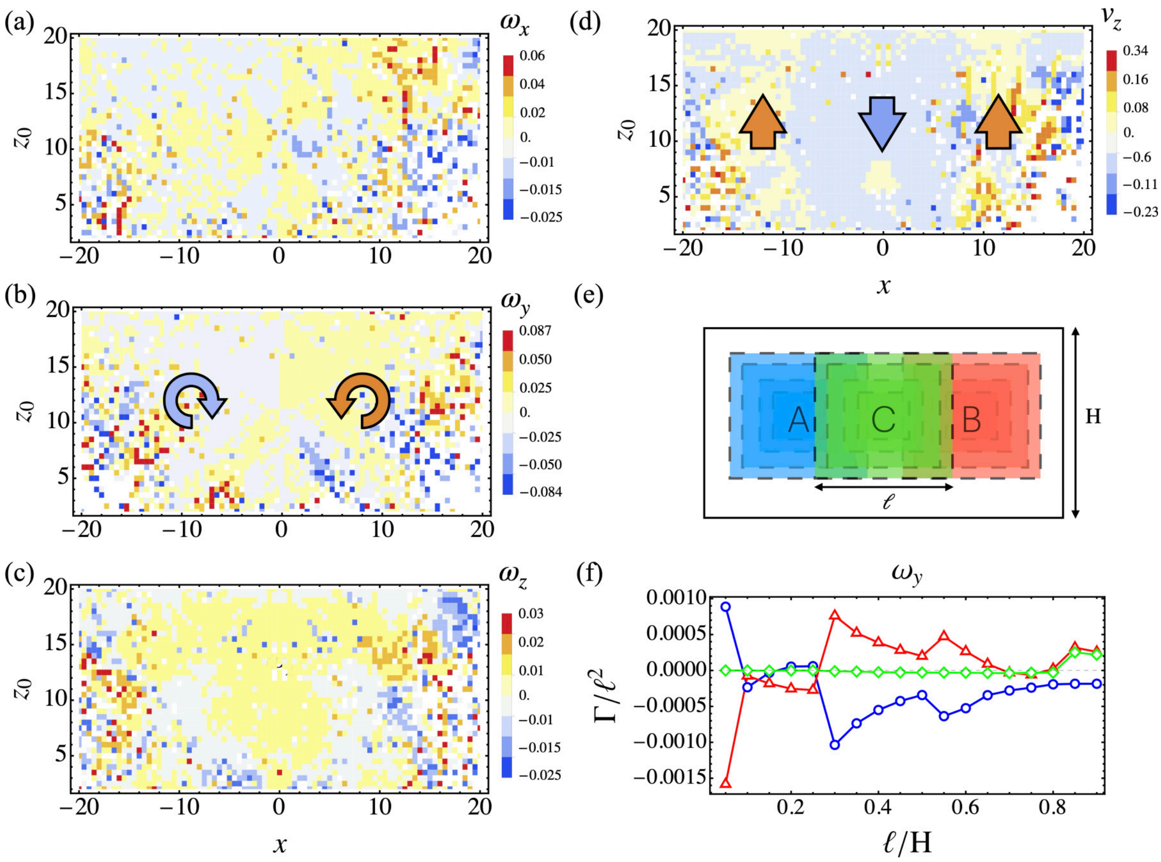

FIG. 5. *Active carpets* can drive large-scale recirculations. [(a)–(c)] Average vorticity exerted by an *active carpet* on fluid parcels across the confinement space, in the plane x-z, for puller microswimmers $H = 20$, $\lambda = 1.5$, $\kappa = -30$, and $\sigma = 1$. The color code for vertical flows is the following: clockwise rotations (blue) and counterclockwise rotations (red); the magnitude of the vorticity is indicated in the legends of each component. (d) The average vertical flow in the examined region. The orange and blue arrows show the direction of the mean flow. (e) Regions A, B, and C were used to evaluate the circulation Eq. (13) over the confinement space. Squares with side ℓ were utilized in each area to measure the circulation. (f) Circulation Γ is associated with the vorticity in the y direction, divided by the area ℓ^2.

distinct spatial regions: (I) a region close to the *active carpet* where vertical fluctuations dominate, (II) an intermediate region characterized by isotropic hydrodynamic fluctuations, and (III) a distal region where horizontal fluctuations surpass vertical ones. This understanding offers a method to control directed motion within confined vertical spaces and demonstrates how both dependencies affect the amplification or reduction of agitation regions.

(3) By measuring the velocity pair correlation of the hydrodynamic fluctuations induced by the confined *active carpet*, we demonstrated the existence of coherent vortical motion, primarily driven by vertical flows. Our investigation revealed that the characteristic length of the roll-like patterns formed is closely linked to the thickness of the confined layer hosting the *active carpet*. These coherent vortical structures become especially prominent in systems with strong confinement and sharp viscosity gradients at the fluid-fluid interface.

These findings carry implications for our comprehension of microbial swimmers that flourish and cultivate biofilms at interfaces in natural shallow water environments [4], such as (i) ponds etched on soil and ice [98,99], (ii) shallow saline lagoons and wetlands [100], (iii) streams [101], inside the human body [14,102], and even in human habitats like the thin films of water found in kitchens, bathrooms, swimming pools, and laboratories [103,104].

By shedding light on the dynamics of these active flows, our research offers insights into the behavior of microbial communities in thin layers within aquatic ecosystems. From pristine natural settings to human-altered landscapes, the understanding of the hydrodynamics induced by *active carpets* is crucial for devising strategies to manage and harness the potential of microbial populations for various applications, ranging from water remediation to microfluidics and biotechnology.

ACKNOWLEDGMENTS

F.A.B., G.A., and F.G.-L. have received support from the ANID–Millennium Science Initiative Program–NCN19 170, Chile. F.G.-L. was supported by Fondecyt Iniciación No. 11220683. This research was partially supported by the supercomputing infrastructure of the NLHPC (CCSS210001). H.N.U. and A.J.T.M.M. were supported by start-up grants from the University of Pennsylvania. A.J.T.M.M. acknowledges funding from the United States Department of Agriculture (USDA-NIFA AFRI Grants No. 2020-67017-30776 and

No. 2020-67015-32330), the Charles E. Kaufman Foundation (Early Investigator Research Award KA2022-129523) and the University of Pennsylvania (University Research Foundation Grant and Klein Family Social Justice Award). Last, we thank the constructive feedback provided by two anonymous referees.

[1] A. V. Kanale, F. Ling, H. Guo, S. Fürthauer, and E. Kanso, Spontaneous phase coordination and fluid pumping in model ciliary carpets, Proc. Natl. Acad. Sci. USA **119**, e2214413119 (2022).

[2] A. J. T. M. Mathijssen, F. Guzmán-Lastra, A. Kaiser, and H. Löwen, Nutrient transport driven by microbial active carpets, Phys. Rev. Lett. **121**, 248101 (2018).

[3] R. V. More and A. M. Ardekani, Motion in stratified fluids, Annu. Rev. Fluid Mech. **55**, 157 (2023).

[4] N. Desai and A. M. Ardekani, Biofilms at interfaces: Microbial distribution in floating films, Soft Matter **16**, 1731 (2020).

[5] L. Vaccari, M. Molaei, T. H. Niepa, D. Lee, R. L. Leheny, and K. J. Stebe, Films of bacteria at interfaces, Adv. Colloid Interface Sci. **247**, 561 (2017).

[6] A. Ahmadzadegan, S. Wang, P. P. Vlachos, and A. M. Ardekani, Hydrodynamic attraction of bacteria to gas and liquid interfaces, Phys. Rev. E **100**, 062605 (2019).

[7] D. Pimponi, M. Chinappi, P. Gualtieri, and C. M. Casciola, Hydrodynamics of flagellated microswimmers near free-slip interfaces, J. Fluid Mech. **789**, 514 (2016).

[8] J. Elgeti and G. Gompper, Microswimmers near surfaces, Eur. Phys. J.: Spec. Top. **225**, 2333 (2016).

[9] A. J. Mathijssen, A. Doostmohammadi, J. M. Yeomans, and T. N. Shendruk, Hydrodynamics of micro-swimmers in films, J. Fluid Mech. **806**, 35 (2016).

[10] B. Chakrabarti, M. Rachh, S. Y. Shvartsman, and M. J. Shelley, Cytoplasmic stirring by active carpets, Proc. Nat. Acad. Sci. USA **121**, e2405114121 (2024).

[11] W. Gilpin, M. S. Bull, and M. Prakash, The multiscale physics of cilia and flagella, Nat. Rev. Phys. **2**, 74 (2020).

[12] S. Espada Burriel and R. Colin, Active density pattern formation in bacterial binary mixtures, PRX Life **2**, 023002 (2024).

[13] Y. Hosaka, R. Golestanian, and A. Daddi-Moussa-Ider, Hydrodynamics of an odd active surfer in a chiral fluid, New J. Phys. **25**, 083046 (2023).

[14] A. J. Maheshwari, A. M. Sunol, E. Gonzalez, D. Endy, and R. N. Zia, Colloidal hydrodynamics of biological cells: A frontier spanning two fields, Phys. Rev. Fluids **4**, 110506 (2019).

[15] W. M. Durham and R. Stocker, Thin phytoplankton layers: Characteristics, mechanisms, and consequences, Annu. Rev. Mar. Sci. **4**, 177 (2012).

[16] Ò. Guadayol, T. Mendonca, M. Segura-Noguera, A. J. Wright, M. Tassieri, and S. Humphries, Microrheology reveals microscale viscosity gradients in planktonic systems, Proc. Natl. Acad. Sci. USA **118**, e2011389118 (2021).

[17] M. R. Stehnach, N. Waisbord, D. M. Walkama, and J. S. Guasto, Viscophobic turning dictates microalgae transport in viscosity gradients, Nat. Phys. **17**, 926 (2021).

[18] M. Cohen, J. Kofonow, J. V. Nayak, J. N. Palmer, A. G. Chiu, J. G. Leid, and N. A. Cohen, Biofilms in chronic rhinosinusitis: A review, Am. J. Rhinol. Allergy **23**, 255 (2009).

[19] K. L. Visick, M. A. Schembri, F. Yildiz, and J.-M. Ghigo, Biofilms 2015: Multidisciplinary approaches shed light into microbial life on surfaces, J. Bacteriol. **198**, 2553 (2016).

[20] R. Stocker, Marine microbes see a sea of gradients, Science **338**, 628 (2012).

[21] R. Bearon and D. Grünbaum, Bioconvection in a stratified environment: Experiments and theory, Phys. Fluids **18**, 127102 (2006).

[22] M. A. Bees, Advances in bioconvection, Annu. Rev. Fluid Mech. **52**, 449 (2020).

[23] A. Théry, L. Le Nagard, J.-C. Ono-dit Biot, C. Fradin, K. Dalnoki-Veress, and E. Lauga, Self-organisation and convection of confined magnetotactic bacteria, Sci. Rep. **10**, 13578 (2020).

[24] A. Théry, A. Chamolly, and E. Lauga, Controlling confined collective organization with taxis, Phys. Rev. Lett. **132**, 108301 (2024).

[25] B. Vincenti, G. Ramos, M. L. Cordero, C. Douarche, R. Soto, and E. Clement, Magnetotactic bacteria in a droplet self-assemble into a rotary motor, Nat. Commun. **10**, 5082 (2019).

[26] D. J. Carlson, Viscosity of sea-surface slicks, Nature (London) **329**, 823 (1987).

[27] J. M. Sieburth and J. T. Conover, Slicks associated with *Trichodesmium* blooms in the Sargasso sea, Nature (London) **205**, 830 (1965).

[28] L. Voskuhl and J. Rahlff, Natural and oil surface slicks as microbial habitats in marine systems: A mini review, Front. Mar. Sci. **9**, 1020843 (2022).

[29] O. Wurl, C. Stolle, C. Van Thuoc, P. T. Thu, and X. Mari, Biofilm-like properties of the sea surface and predicted effects on air–sea Co_2 exchange, Prog. Oceanogr. **144**, 15 (2016).

[30] M. Cunliffe, R. C. Upstill-Goddard, and J. C. Murrell, Microbiology of aquatic surface microlayers, FEMS Microbiol. Rev. **35**, 233 (2011).

[31] Z. Zhang, L. Liu, C. Liu, and W. Cai, Studies on the sea surface microlayer: II. the layer of sudden change of physical and chemical properties, J. Colloid Interface Sci. **264**, 148 (2003).

[32] M. Cunliffe, A. Engel, S. Frka, B. Gašparović, C. Guitart, J. C. Murrell, M. Salter, C. Stolle, R. Upstill-Goddard, and O. Wurl, Sea surface microlayers: A unified physicochemical and biological perspective of the air–ocean interface, Prog. Oceanogr. **109**, 104 (2013).

[33] J. Deng, M. Molaei, N. G. Chisholm, and K. J. Stebe, Motile bacteria at oil–water interfaces: *Pseudomonas aeruginosa*, Langmuir **36**, 6888 (2020).

[34] G. Subbiahdoss and E. Reimhult, Biofilm formation at oil-water interfaces is not a simple function of bacterial hydrophobicity, Colloids Surf. B **194**, 111163 (2020).

[35] S. Simoncelli, S. J. Thackeray, and D. J. Wain, Can small zooplankton mix lakes? Limnol. Oceanogr. Lett. **2**, 167 (2017).

[36] E. Kunze, Biologically generated mixing in the ocean, Annu. Rev. Mar. Sci. **11**, 215 (2019).

[37] A. M. Ardekani and R. Stocker, Stratlets: Low Reynolds number point-force solutions in a stratified fluid, Phys. Rev. Lett. **105**, 084502 (2010).
[38] G. L. Wagner, W. R. Young, and E. Lauga, Mixing by microorganisms in stratified fluids, J. Mar. Res. **72**, 47 (2014).
[39] D. Noto and H. N. Ulloa, Simple tracking of occluded self-propelled organisms, Meas. Sci. Technol. **35**, 035705 (2024).
[40] I. A. Houghton, J. R. Koseff, S. G. Monismith, and J. O. Dabiri, Vertically migrating swimmers generate aggregation-scale eddies in a stratified column, Nature (London) **556**, 497 (2018).
[41] I. A. Houghton and J. O. Dabiri, Alleviation of hypoxia by biologically generated mixing in a stratified water column, Limnol. Oceanogr. **64**, 2161 (2019).
[42] R. Ouillon, I. Houghton, J. Dabiri, and E. Meiburg, Active swimmers interacting with stratified fluids during collective vertical migration, J. Fluid Mech. **902**, A23 (2020).
[43] A. Morozov and D. Marenduzzo, Enhanced diffusion of tracer particles in dilute bacterial suspensions, Soft Matter **10**, 2748 (2014).
[44] G. Miño, J. Dunstan, A. Rousselet, E. Clément, and R. Soto, Induced diffusion of tracers in a bacterial suspension: Theory and experiments, J. Fluid Mech. **729**, 423 (2013).
[45] T. Sommer, F. Danza, J. Berg, A. Sengupta, G. Constantinescu, T. Tokyay, H. Bürgmann, Y. Dressler, O. Sepúlveda Steiner, C. Schubert *et al.*, Bacteria-induced mixing in natural waters, Geophys. Res. Lett. **44**, 9424 (2017).
[46] A. J. T. M. Mathijssen, R. Jeanneret, and M. Polin, Universal entrainment mechanism controls contact times with motile cells, Phys. Rev. Fluids **3**, 033103 (2018).
[47] O. S. Steiner, D. Bouffard, and A. Wüest, Persistence of bioconvection-induced mixed layers in a stratified lake, Limnol. Oceanogr. **66**, 1531 (2021).
[48] S. Simoncelli, S. J. Thackeray, and D. J. Wain, On biogenic turbulence production and mixing from vertically migrating zooplankton in lakes, Aquat. Sci. **80**, 35 (2018).
[49] R. Ran, Q. Brosseau, B. C. Blackwell, B. Qin, R. L. Winter, and P. E. Arratia, Bacteria hinder large-scale transport and enhance small-scale mixing in time-periodic flows, Proc. Natl. Acad. Sci. USA **118**, e2108548118 (2021).
[50] J. Singh, A. E. Patteson, B. O. T. Maldonado, P. K. Purohit, and P. E. Arratia, Bacterial activity hinders particle sedimentation, Soft Matter **17**, 4151 (2021).
[51] V. Škultéty, D. Bárdfalvy, J. Stenhammar, C. Nardini, and A. Morozov, Hydrodynamic instabilities in a 2-D sheet of microswimmers embedded in a 3-D fluid, arXiv:2302.13966 [J. Fluid Mech. (to be published)].
[52] S. Belan and M. Kardar, Pair dispersion in dilute suspension of active swimmers, J. Chem. Phys. **150**, 064907 (2019).
[53] G. Aguayo, A. J. Mathijssen, H. N. Ulloa, R. Soto, and F. Guzman-Lastra, Floating active carpets drive transport and aggregation in aquatic ecosystems, J. Fluid Mech. **995**, A16 (2024).
[54] S. Gokhale, J. Li, A. Solon, J. Gore, and N. Fakhri, Dynamic clustering of passive colloids in dense suspensions of motile bacteria, Phys. Rev. E **105**, 054605 (2022).
[55] P. Kushwaha, V. Semwal, S. Maity, S. Mishra, and V. Chikkadi, Phase separation of passive particles in active liquids, Phys. Rev. E **108**, 034603 (2023).
[56] R. Großmann, L. S. Bort, T. Moldenhawer, M. Stange, S. S. Panah, R. Metzler, and C. Beta, Non-gaussian displacements in active transport on a carpet of motile cells, Phys. Rev. Lett. **132**, 088301 (2024).
[57] F. Guzmán-Lastra, H. Löwen, and A. J. Mathijssen, Active carpets drive non-equilibrium diffusion and enhanced molecular fluxes, Nat. Commun. **12**, 1906 (2021).
[58] X. Zhang, J. Guo, X. Fu, D. Zhang, and Y. Zhao, Tailoring flexible arrays for artificial cilia actuators, Adv. Intell. Syst. **3**, 2000225 (2021).
[59] A. H. Gelebart, M. Mc Bride, A. P. Schenning, C. N. Bowman, and D. J. Broer, Photoresponsive fiber array: Toward mimicking the collective motion of cilia for transport applications, Adv. Funct. Mater. **26**, 5322 (2016).
[60] Y. Wang, J. den Toonder, R. Cardinaels, and P. Anderson, A continuous roll-pulling approach for the fabrication of magnetic artificial cilia with microfluidic pumping capability, Lab Chip **16**, 2277 (2016).
[61] F. Meng, D. Matsunaga, J. M. Yeomans, and R. Golestanian, Magnetically actuated artificial cilium: A simple theoretical model, Soft Matter **15**, 3864 (2019).
[62] V. V. Khatavkar, P. D. Anderson, J. M. den Toonder, and H. E. Meijer, Active micromixer based on artificial cilia, Phys. Fluids **19**, 083605 (2007).
[63] K. Aderogba and J. Blake, Action of a force near the planar surface between two semi-infinite immiscible liquids at very low Reynolds numbers, Bull. Austr. Math. Soc. **18**, 345 (1978).
[64] G. I. Taylor, Analysis of the swimming of microscopic organisms, Proc. R. Soc. Lond. A **209**, 447 (1951).
[65] E. M. Purcell, Life at low Reynolds number, Am. J. Phys. **45**, 3 (1977).
[66] G. G. Stokes, *On the Effect of the Internal Friction of Fluids on the Motion of Pendulums* (Pitt Press, Cambridge, 1851).
[67] G. Hancock, The self-propulsion of microscopic organisms through liquids, Proc. R. Soc. Lond. A **217**, 96 (1953).
[68] J. Happel and H. Brenner, *Low Reynolds Number Hydrodynamics: With Special Applications to Particulate Media* (Springer Science & Business Media, New York, 2012), Vol. 1.
[69] S. Kim and S. J. Karrila, *Microhydrodynamics: Principles and Selected Applications* (Dover, Mineola, NY, 2013).
[70] A. J. Mathijssen, D. O. Pushkin, and J. M. Yeomans, Tracer trajectories and displacement due to a micro-swimmer near a surface, J. Fluid Mech. **773**, 498 (2015).
[71] S. E. Spagnolie and E. Lauga, Hydrodynamics of self-propulsion near a boundary: Predictions and accuracy of far-field approximations, J. Fluid Mech. **700**, 105 (2012).
[72] A. T. Chwang and T. Y.-T. Wu, Hydromechanics of low-Reynolds-number flow. Part 2. Singularity method for stokes flows, J. Fluid Mech. **67**, 787 (1975).
[73] G. Batchelor, The stress system in a suspension of force-free particles, J. Fluid Mech. **41**, 545 (1970).
[74] K. Drescher, R. E. Goldstein, N. Michel, M. Polin, and I. Tuval, Direct measurement of the flow field around swimming microorganisms, Phys. Rev. Lett. **105**, 168101 (2010).
[75] M. Hondzo, J. You, J. Taylor, G. Bartlet, and V. R. Voller, Measurement and scaling of lake surface skin temperatures, Geophys. Res. Lett. **49**, e2021GL093226 (2022).

[76] V. A. Shaik and G. J. Elfring, Hydrodynamics of active particles in viscosity gradients, Phys. Rev. Fluids **6**, 103103 (2021).

[77] M. G. Petrino and R. Doetsch, 'Viscotaxis', a new behavioural response of *Leptospira interrogans (biflexa)* strain b16, Microbiology **109**, 113 (1978).

[78] M. Y. Sherman, E. Timkina, and A. Glagolev, Viscosity taxis in *Escherichia coli*, FEMS Microbiol. Lett. **13**, 137 (1982).

[79] C. Datt and G. J. Elfring, Active particles in viscosity gradients, Phys. Rev. Lett. **123**, 158006 (2019).

[80] B. Liebchen, P. Monderkamp, B. ten Hagen, and H. Löwen, *Viscotaxis*: Microswimmer navigation in viscosity gradients, Phys. Rev. Lett. **120**, 208002 (2018).

[81] Marcos, H. C. Fu, T. R. Powers, and R. Stocker, Bacterial rheotaxis, Proc. Natl. Acad. Sci. USA **109**, 4780 (2012).

[82] G. Ramos, M. L. Cordero, and R. Soto, Bacteria driving droplets, Soft Matter **16**, 1359 (2020).

[83] C. Villalobos, M. L. Cordero, E. Clément, and R. Soto, Recovering the activity parameters of an active fluid confined in a sphere, arXiv:2403.11933.

[84] N. Desai and A. M. Ardekani, Modeling of active swimmer suspensions and their interactions with the environment, Soft Matter **13**, 6033 (2017).

[85] L. Zeng, W. Jiang, and T. J. Pedley, Sharp turns and gyrotaxis modulate surface accumulation of microorganisms, Proc. Natl. Acad. Sci. USA **119**, e2206738119 (2022).

[86] See Supplemental Material at http://link.aps.org/supplemental/10.1103/PhysRevResearch.7.013152 for further details on the definition of an active carpet, and some additional figures for different active carpets configurations that are not required to understanding the main text.

[87] K. Drescher, J. Dunkel, L. H. Cisneros, S. Ganguly, and R. E. Goldstein, Fluid dynamics and noise in bacterial cell–cell and cell–surface scattering, Proc. Natl. Acad. Sci. USA **108**, 10940 (2011).

[88] M. M. Mrokowska, A. Krztoń-Maziopa, and M. Dbowski, Effect of exopolymer gels on the viscoelasticity of mucus-rich saltwater and settling dynamics of particles, Mar. Chem. **246**, 104163 (2022).

[89] M. G. Mazza, The physics of biofilms—An introduction, J. Phys. D **49**, 203001 (2016).

[90] D. Noto, J. A. Letelier, and H. N. Ulloa, Plume-scale confinement on thermal convection, Proc. Natl. Acad. Sci. USA **121**, e2403699121 (2024).

[91] B. F. Castro, M. Peña, E. Nogueira, M. Gilcoto, E. Broullón, A. Comesaña, D. Bouffard, A. C. Naveira Garabato, and B. Mouriño-Carballido, Intense upper ocean mixing due to large aggregations of spawning fish, Nature Geosci. **15**, 287 (2022).

[92] J. Tamayo, Y. Zhang, M. E. Asp, A. Patteson, A. M. Ardekani, and A. Gopinath, Swarming bacterial fronts: Dynamics and morphology of active swarm interfaces propagating through passive frictional domains, Biophys. J. **123**, 541a (2024).

[93] D. Bárdfalvy, V. Škultéty, C. Nardini, A. Morozov, and J. Stenhammar, Collective motion in a sheet of microswimmers, Commun. Phys. **7**, 93 (2024).

[94] D. Mondal, A. G. Prabhune, S. Ramaswamy, and P. Sharma, Strong confinement of active microalgae leads to inversion of vortex flow and enhanced mixing, Elife **10**, e67663 (2021).

[95] M. Akashi, T. Yanagisawa, Y. Tasaka, T. Vogt, Y. Murai, and S. Eckert, Transition from convection rolls to large-scale cellular structures in turbulent Rayleigh-Bénard convection in a liquid metal layer, Phys. Rev. Fluids **4**, 033501 (2019).

[96] D. Noto, H. N. Ulloa, and J. A. Letelier, Reconstructing temperature fields for thermally-driven flows under quasi-steady state, Exp. Fluids **64**, 74 (2023).

[97] A. J. T. M. Mathijssen, M. Lisicki, V. N. Prakash, and E. J. L. Mossige, Culinary fluid mechanics and other currents in food science, Rev. Mod. Phys. **95**, 025004 (2023).

[98] V. Mohit, A. Culley, C. Lovejoy, F. Bouchard, and W. F. Vincent, Hidden biofilms in a far northern lake and implications for the changing arctic, npj Biofilms Microbiomes **3**, 17 (2017).

[99] A. M. Anesio, S. Lutz, N. A. Chrismas, and L. G. Benning, The microbiome of glaciers and ice sheets, npj Biofilms Microbiomes **3**, 10 (2017).

[100] A. de la Fuente, Heat and dissolved oxygen exchanges between the sediment and water column in a shallow salty lagoon, J. Geophys. Res. Biogeosci. **119**, 596 (2014).

[101] T. J. Battin, K. Besemer, M. M. Bengtsson, A. M. Romani, and A. I. Packmann, The ecology and biogeochemistry of stream biofilms, Nat. Rev. Microbiol. **14**, 251 (2016).

[102] N. Figueroa-Morales, L. Dominguez-Rubio, T. L. Ott, and I. S. Aranson, Mechanical shear controls bacterial penetration in mucus, Sci. Rep. **9**, 9713 (2019).

[103] G. E. Flores, S. T. Bates, J. G. Caporaso, C. L. Lauber, J. W. Leff, R. Knight, and N. Fierer, Diversity, distribution and sources of bacteria in residential kitchens, Environ. Microbiol. **15**, 588 (2013).

[104] M. Novak Babič, C. Gostinčar, and N. Gunde-Cimerman, Microorganisms populating the water-related indoor biome, Appl. Microbiol. Biotechnol. **104**, 6443 (2020).